Comparative study of constitutive and finite element formulations for large strain elastoplasticity

Laurent Stainier, Claudio Careglio, Carlos Garcia-Garino, Anibal Mirasso

COMPARATIVE STUDY OF CONSTITUTIVE AND FINITE ELEMENT FORMULATIONS FOR LARGE STRAIN ELASTOPLASTICITY

Laurent Stainier[a,b], Claudio Careglio[c], Carlos Garcia-Garino[c,d] and Anibal Mirasso[c,e]

[a]*LTAS-MCT, Département Aérospatiale & Mécanique, Université de Liège, Chemin des chevreuils 1, 4000 Liège, Belgium,* http://www.ltas-mct.ulg.ac.be/
[b]*Research Associate, Fonds National de la Recherche Scientifique, Belgium*
[c]*LAPIC, Instituto Tecnológico Universitario, Universidad Nacional de Cuyo, Argentina,* http://www.itu.uncu.edu.ar/
[d]*CONICET: Miembro carrera de Investigador Cientifico*
[e]*Facultad de Ingeniería, Universidad Nacional de Cuyo, Mendoza, Argentina,* http://www.uncu.edu.ar/

Keywords: Computational Plasticity.

Abstract. This paper presents a comparative study of the different formulations used in research groups in Liège and Mendoza, for the modelling of large plastic deformations. The comparison focused on a few academic standardized problems. We analysed both the constitutive formulation (strain-stress relations) and the finite element formulation (discretized mechanical balance equations).

In particular, we compared two constitutive formulations, both hyperelastic, but resulting from different theoretical approaches. We also compared different types of finite elements (4-noded quadrangles and 6-noded triangles), in axisymmetric and plane strain settings.

These comparisons show that both approaches yield very similar results. Computations also show that models based on 6-noded triangles give good results. The only limitation suggested by the results obtained is that triangles appear to be more sensitive to large distorsions than quadrangles.

1 INTRODUCTION

Two different constitutive formulations were considered here: that of ZorgLib and that of SOGDE. The formulation used in ZorgLib is described in details in Ortiz and Stainier (1999). It is a fully variational formulation, based on the minimization of an incremental energy, and set in a total Lagrangean hyperelastic framework. The formulation used in SOGDE is described in details in García-Garino (1993). This formulation is set in an updated Lagrangean hyperelastic framework. Among the main differences between the two formulations, one can note that in ZorgLib, the plastic consistency condition is written in the intermediate configuration (no elastic deformation), while in SOGDE it is written in the deformed configuration.

The finite element formulations used differ only in the case of bilinear quadrangles. Indeed, in this case, particular caution must be taken in dealing with plastic incompressibility. In ZorgLib, the formulation is based on a potential energy variational principle, augmented with an additional term involving piecewise-constant pressure and volumic deformation fields. The formulation in SOGDE is slightly different, in that it does not follow strictly the variational principle, but uses adhoc procedures in some of its parts.

For the quadratic 6-noded triangle, a standard isoparametric formulation (with 3 Gauss points) is used in all cases.

2 FINITE DEFORMATIONS KINEMATICS

The kinematics of the problem is based on the very well known multiplicative decomposition of deformation gradient tensor $\boldsymbol{F}$ in its elastic and plastic components (initially proposed by Lee (1969) and since used by many others), as can be seen in Figure 1 where the intermediate configuration is shown.

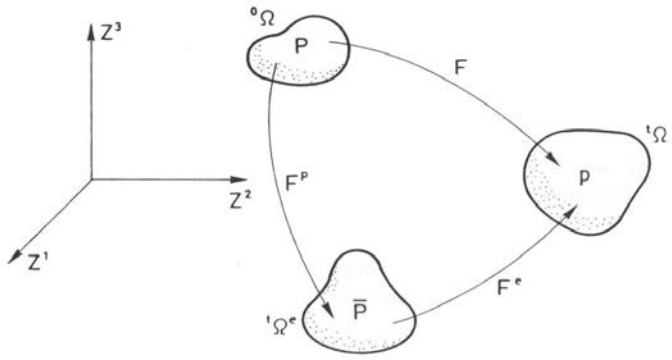

Figure 1: Kinematics of large strain elastoplastic solid: configurations

$$\boldsymbol{F} \;=\; \boldsymbol{F}^e\,\boldsymbol{F}^p \tag{1}$$

The right Cauchy-Green tensor $\boldsymbol{C}$ as well as corresponding elastic $\boldsymbol{C}^e$ and plastic $\boldsymbol{C}^p$ tensors respectively (Green and Nagdhi, 1965; Simo and Ortiz, 1985) are defined in eq. (2):

$$\begin{aligned} \boldsymbol{C} &= \boldsymbol{F}^T\,\boldsymbol{F} \\ \boldsymbol{C}^e &= \boldsymbol{F}^{eT}\,\boldsymbol{F}^e \\ \boldsymbol{C}^p &= \boldsymbol{F}^{pT}\,\boldsymbol{F}^p \end{aligned} \tag{2}$$

The Green Lagrange tensor $\boldsymbol{E}$ as well as the plastic and elastic Green Lagrange tensors$\boldsymbol{E}^p$ and $\boldsymbol{E}^e$ can be written in terms of the right Cauchy Green tensors and metric tensors $\boldsymbol{G}$ and $\bar{\boldsymbol{G}}$ in material and intermediate configurations respectively.

$$\begin{aligned}\boldsymbol{E} &= \frac{1}{2}(\boldsymbol{C} - \boldsymbol{G}) \\ \boldsymbol{E}^e &= \frac{1}{2}(\boldsymbol{C}^e - \bar{\boldsymbol{G}}) \\ \boldsymbol{E}^p &= \frac{1}{2}(\boldsymbol{C}^p - \boldsymbol{G})\end{aligned} \tag{3}$$

where $\boldsymbol{G}$ and $\bar{\boldsymbol{G}}$ are the metric tensors in the material and intermediate configurations, ${}^o\Omega$ and ${}^t\Omega^e$ respectively.

It is important to note that while tensors $\boldsymbol{C}$,$\boldsymbol{C}^p$,$\boldsymbol{E}$ and $\boldsymbol{E}^p$ are defined in the material configuration, $\boldsymbol{C}^e$ and $\boldsymbol{E}^e$ are defined in the intermediate configuration. A detailed overview of the kinematics of solids under large strain can be seen in García-Garino (1993); Simo and Ortiz (1985).

In the deformed configuration is defined the Almansi strain tensor $\boldsymbol{e}$ and its elastic and plastic components $\boldsymbol{e}^e$ and $\boldsymbol{e}^p$, respectively, in terms of the spatial metric tensor $\boldsymbol{g}$, the finger tensor $\boldsymbol{b}^{-1}$ and its elastic component $\boldsymbol{b}^{e-1}$, as can be seen in equations (4) and (5).

$$\begin{aligned}\boldsymbol{b}^{-1} &= \boldsymbol{F}^{-T}\,\boldsymbol{F}^{-1} \\ \boldsymbol{b}^{e-1} &= \boldsymbol{F}^{e-T}\,\boldsymbol{F}^{e-1}\end{aligned} \tag{4}$$

$$\begin{aligned}\boldsymbol{e} &= \frac{1}{2}\,(\boldsymbol{g} \;-\; \boldsymbol{b}^{-1}) \\ \boldsymbol{e}^e &= \frac{1}{2}\,(\boldsymbol{g} \;-\; \boldsymbol{b}^{e-1}) \\ \boldsymbol{e}^p &= \boldsymbol{e} \;-\; \boldsymbol{e}^e\end{aligned} \tag{5}$$

In recent literature of large deformation mechanics, push-forward ϕ_* and pull-back ϕ^* operators (see Marsden and Hughes (1983)) are often used in order to transform strain tensors between the different configurations:

$$\begin{aligned}\boldsymbol{E} &= \phi^*\boldsymbol{e} \\ \boldsymbol{C} &= \phi^*\boldsymbol{g} \\ \boldsymbol{b}^{-1} &= \phi_*\boldsymbol{G} \\ \boldsymbol{E}^e &= \phi^{*e}\boldsymbol{e} \\ \boldsymbol{b}^{e-1} &= \phi^e_*\bar{\boldsymbol{G}}\end{aligned} \tag{6}$$

where ϕ^* ϕ_* and ϕ^{*e} ϕ^e_* are associated to $\boldsymbol{F}$ and $\boldsymbol{F}^e$ deformation gradients respectively. A detailed overview of this relations can be seen in García-Garino (1993).

The velocity gradient tensor in deformed configuration and its plastic counterpart in intermediate configuration, given in equations (7) and (8) respectively, are used to characterize material and plastic flow in constitutive equations:

$$\boldsymbol{l} = \dot{\boldsymbol{F}}\boldsymbol{F}^{-1} \tag{7}$$

$$\boldsymbol{L}^p = \dot{\boldsymbol{F}}^p\boldsymbol{F}^{p-1} \tag{8}$$

The rate of deformation tensors $\boldsymbol{d}$ and $\boldsymbol{D}^p$ are the symmetric component of the velocities gradient tensor $\boldsymbol{l}$ in the current configuration ${}^t\Omega$ and $\boldsymbol{L}^p$ in the intermediate configuration ${}^t\Omega^e$ respectively. Alternatively, rate of deformation tensors can be computed as the Lie derivatives L_v of deformation tensors (Marsden and Hughes, 1983).

3 HYPERELASTIC FORMULATION OF FINITE PLASTICITY

In this section a constitutive model able to model the behaviour of large strain elastoplastic solids proposed by García-Garino (1993); García-Garino and Oliver (1995) is briefly presented here. The model is fully consistent with Continuum Mechanics and is derived in the context Internal Variables theory.

3.1 Constitutive Model

3.1.1 Derivation of the model in the intermediate configuration

The free energy function is written in the intermediate configuration ${}^t\Omega^e$ as:

$$\Phi = \Phi(\boldsymbol{F}, \boldsymbol{F}^p, \boldsymbol{\Lambda}) \tag{9}$$

where $\boldsymbol{\Lambda}$ is a set of internal variables that accounts for plasticity effects, like hardening for instance. Taking into account the multiplicative decomposition of deformation gradient tensor given in (1) can be written $\boldsymbol{F}^e = \boldsymbol{F}^e(\boldsymbol{F}, \boldsymbol{F}^p)$, and equation (9 results:

$$\hat{\Phi} = \hat{\Phi}(\boldsymbol{F}^e, \boldsymbol{\Lambda}) \tag{10}$$

It is important to note that the presence of $\boldsymbol{F}^p$ as an argument of free energy function can be necessary in order to model kinematic hardening. In order to satisfy objectivity the dependence of $\hat{\Phi}$ on $\boldsymbol{F}^e$ is taken into account including a symmetric tensor like the elastic right stretch tensor $\boldsymbol{U}^e$, or other strain tensors like $\boldsymbol{C}^e$ or $\boldsymbol{E}^e$

$$\hat{\Phi} = \hat{\Phi}(\boldsymbol{F}^e, \boldsymbol{\Lambda}) = \bar{\Phi}(\boldsymbol{U}^e, \boldsymbol{\Lambda}) = \tilde{\Phi}(\boldsymbol{C}^e, \boldsymbol{\Lambda}) = \varphi(\boldsymbol{E}^e, \boldsymbol{\Lambda}) \tag{11}$$

Under *uncoupled elasticity* hypothesis, the free energy function can be expressed as the sum of its elastic and plastic components:

$$\varphi = \varphi^e + \varphi^p = \varphi^e(\boldsymbol{E}^e) + \varphi^p(\boldsymbol{\Lambda}) \tag{12}$$

The additive decomposition of the free energy in an elastic part φ^e and a plastic part φ^p translates the fact that the elastic response of some materials is independent of the internal processes of plasticity, like is the case of metals for instance.

Plastic and Yield functions are written in the strain space. In order to satisfy the *P*rinciple of Equipresence (Malvern, 1969) the same arguments of free energy function are included:

$$\hat{F} = \hat{F}(\boldsymbol{E}^e, \boldsymbol{\Lambda}) \tag{13}$$

$$\hat{G} = \hat{G}(\boldsymbol{E}^e, \boldsymbol{\Lambda}) \tag{14}$$

The plastic component of rate of deformation tensor $\boldsymbol{D}^p$ is considered as the flow rule of the model. This assumption has the inconvenience to define the intermediate configuration up to an undefined rigid rotation, however if isotropic models are used this drawback has no effect.

The evolution law of internal variables $\dot{\boldsymbol{\Lambda}}$ is written in terms of the flow rule as:

$$\dot{\boldsymbol{\Lambda}} \stackrel{\text{def}}{=} \boldsymbol{H}(\boldsymbol{E}^e, \boldsymbol{\Lambda}) \cdot \boldsymbol{D}^p \tag{15}$$

where $\boldsymbol{H}$ is a proper tensor.

The stress tensor in the intermediate configuration can be computed from the elastic component of free energy function as:

$$\boldsymbol{S} = \rho_o \frac{\partial \varphi^e(\boldsymbol{E}^e)}{\partial \boldsymbol{E}^e} \tag{16}$$

The fourth order tangent elasticity tensor results from equation (16):

$$\boldsymbol{A}^e = \rho_o \frac{\partial^2 \varphi^e(\boldsymbol{E}^e)}{\partial \boldsymbol{E}^e \otimes \partial \boldsymbol{E}^e} \tag{17}$$

From the hyperelastic constitutive equation (16) the elastic tensor $\boldsymbol{E}^e$ can be rewritten in terms of stress tensor $\boldsymbol{S}$. Then yield and potential functions given in equations (13) and (14) can be expressed in stress space as:

$$G = G(\boldsymbol{S}(\boldsymbol{E}^e), \boldsymbol{\Lambda}) \tag{18}$$

$$F = F(\boldsymbol{S}(\boldsymbol{E}^e), \boldsymbol{\Lambda}) \tag{19}$$

The flow rule $\boldsymbol{D}^p$ can be written in the stress space in terms of the Plastic Potential function G as:

$$\boldsymbol{D}^p \;\propto\; \frac{\partial G(\boldsymbol{S}, \boldsymbol{\Lambda})}{\partial \boldsymbol{S}} \tag{20}$$

From the plastic consistency condition $\dot{F}$ written in the intermediate configuration the elastoplastic fourth order constitutive tensor results:

$$L_v^p(\boldsymbol{S}) = \left[\boldsymbol{A}^e - \frac{\{\dfrac{\partial F}{\partial \boldsymbol{S}} : \boldsymbol{A}^e\} \otimes \{\boldsymbol{A}^e : \dfrac{\partial G}{\partial \boldsymbol{S}}\}}{\dfrac{\partial F}{\partial \boldsymbol{S}} : \boldsymbol{A}^e : \dfrac{\partial G}{\partial \boldsymbol{S}} + H} \right] : \boldsymbol{D} \quad L_v^p(\boldsymbol{S}) = \boldsymbol{A} : \boldsymbol{D} \tag{21}$$

where has been taken into account that for a scalar function (like F in this case) Lie derivative results $L_v(f) = \dot{f}$ (Marsden and Hughes, 1983; Schutz, 1990)

In order to verify that the Second Law of Thermodynamics is satisfied the Clausius Duhem inequality can be written:

$$\boldsymbol{S} : \boldsymbol{D} - \rho_o \dot{\varphi} \geq 0 \tag{22}$$

if the uncoupled elasticity hypothesis is introduced results:

$$\boldsymbol{S} : \boldsymbol{D} - \rho_o \{\dot{\varphi}^e(\boldsymbol{E}^e) + \dot{\varphi}^p(\boldsymbol{\Lambda})\} \geq 0 \tag{23}$$

taking into account the additive decomposition of rate of deformation tensor $\boldsymbol{D} = \boldsymbol{D}^e + \boldsymbol{D}^p$ at the intermediate configuration eq (23) can be written as an equality given in eq. (24) plus an unequality given in (25), that accounts for the Plastic dissipation D^p as:

$$\boldsymbol{S} : \boldsymbol{D}^e - \rho_o \dot{\varphi}^e(\boldsymbol{E}^e) = 0 \tag{24}$$

$$D^p \stackrel{\text{def}}{=} \boldsymbol{S} : \boldsymbol{D}^p - \rho_o \dot{\varphi}^p(\boldsymbol{\Lambda}) \geq 0 \tag{25}$$

3.1.2 Extension of the model to the deformed configuration

In this section the expresion of the model in the deformed configuration is derived from the results obtained for the intermediate configuration. The Kirchhoff stress tensor can be computed from the Doyle-Ericksen formula (Doyle and Ericksen, 1956). The free energy function φ^e given in eq. (12) is rewritten in terms of spatial variables as:

$$\varphi^e(\boldsymbol{E}^e) \ = \varphi^e(\boldsymbol{F}^{eT} \cdot \boldsymbol{e}^e \cdot \boldsymbol{F}^e) \ = \psi^e(\boldsymbol{e}^e, \boldsymbol{F}^e) \tag{26}$$

Taking into account the chain rule (Lubliner, 1985) results:

$$\frac{\partial \psi^e(\boldsymbol{e}^e, \boldsymbol{F}^e)}{\partial \boldsymbol{e}^e} = \boldsymbol{F}^e \cdot \frac{\partial \varphi^e(\boldsymbol{E}^e)}{\partial \boldsymbol{E}^e} \cdot \boldsymbol{F}^{eT} \tag{27}$$

The Kirchhoff stress tensor $\boldsymbol{\tau}$ can be obtained by computing the push forward of stress tensor $\boldsymbol{\tau} = \phi^e_* \boldsymbol{S}$ to the current configuration:

$$\boldsymbol{\tau} = \phi^e_* \boldsymbol{S} = 2\ \rho_o \boldsymbol{F}^e \cdot \frac{\partial \Psi^e(\boldsymbol{E}^e)}{\partial \boldsymbol{E}^e} \cdot \boldsymbol{F}^{eT} \ = \ 2\ \rho_o\ \frac{\partial \psi^e(\boldsymbol{e}^e, \boldsymbol{F}^e)}{\partial \boldsymbol{e}^e} \tag{28}$$

where eq. (27) has been taken into account.

The elastic tangent tensor in the deformed configuration is obtained computing the elastic push-forward of the tangent elastic tensor in the intermediate configuration $\boldsymbol{a}^e = \phi^e_* \boldsymbol{A}^e$:

$$\boldsymbol{a}^e = \ \rho_o\ \frac{\partial^2 \psi^e(\boldsymbol{e}^e, \boldsymbol{F}^e)}{\partial \boldsymbol{e}^e \otimes \partial \boldsymbol{e}^e} \tag{29}$$

The yield and potential functions become in deformed configuration:

$$g \stackrel{\text{def}}{=} g(\boldsymbol{\tau}, \boldsymbol{\alpha}, \boldsymbol{F}^e) \tag{30}$$

$$f \stackrel{\text{def}}{=} f(\boldsymbol{\tau}, \boldsymbol{\alpha}, \boldsymbol{F}^e) \tag{31}$$

In the derivation of stress tensor from Doyle-Ericcksen formula, material symmetry restriction has not been taken into account. In order to satisfy this requisite $\boldsymbol{F}^e$ is replaced in equations (26,30,31) by the elastic left stretch tensor $\boldsymbol{V}^e$, or another symmetric tensor like the elastic left Cauchy-Green tensor $\boldsymbol{b}^{\#e}$ or the elastic Finger tensor $\boldsymbol{b}^{e-1}$. Then, free energy, plastic potential and yield functions are written as:

$$\psi = \psi^e(\boldsymbol{e}^e, \boldsymbol{b}^{e-1}) + \psi^p(\boldsymbol{\alpha}, \boldsymbol{b}^{e-1}) \tag{32}$$

$$g = g(\boldsymbol{\tau}, \boldsymbol{\alpha}, \boldsymbol{b}^{e-1}) \tag{33}$$

$$f = f(\boldsymbol{\tau}, \boldsymbol{\alpha}, \boldsymbol{b}^{e-1}) \tag{34}$$

The Kirchhoff stress tensor and the fourth order tangent elastic tensor results:

$$\boldsymbol{\tau} = \ \rho_o\ \frac{\partial \psi^e(\boldsymbol{e}^e, \boldsymbol{b}^{e-1})}{\partial \boldsymbol{e}^e} \tag{35}$$

$$\boldsymbol{a}^e = \ \rho_o\ \frac{\partial^2 \psi^e(\boldsymbol{e}^e, \boldsymbol{b}^{e-1})}{\partial \boldsymbol{e}^e \otimes \partial \boldsymbol{e}^e} \tag{36}$$

The elastoplastic tangent tensor in the current configuration is:

$$L_v(\boldsymbol{\tau}) = \left[\boldsymbol{a}^e - \frac{\{\dfrac{\partial f}{\partial \boldsymbol{\tau}} : \boldsymbol{a}^e\} \otimes \{\boldsymbol{a}^e : \dfrac{\partial g}{\partial \boldsymbol{\tau}}\}}{\dfrac{\partial f}{\partial \boldsymbol{\tau}} : \boldsymbol{a}^e : \dfrac{\partial g}{\partial \boldsymbol{\tau}} + H} \right] : \boldsymbol{d} \quad L_v(\boldsymbol{\tau}) \; = \; \boldsymbol{a} : \boldsymbol{d} \tag{37}$$

Plastic dissipation can be computed following a similar procedure to the intermediate configuration:

$$\mathcal{D}^p \stackrel{\text{def}}{=} \boldsymbol{\tau} : \boldsymbol{d}^p + \boldsymbol{p} : \dot{\boldsymbol{\alpha}} \geq 0 \tag{38}$$

where $\boldsymbol{p} = \phi^e_* \bar{\boldsymbol{P}}$ are the conjugate thermodynamic forces to the internal variables: $\boldsymbol{p} = \frac{\partial \psi^p}{\partial \boldsymbol{\alpha}}$.

3.1.3 Application to metals

For the case of metals under large strains, the elastic strains are negligible. In this case the tensor $\boldsymbol{F}^e$ approches to the Identity and Cauchy stress tensor $\boldsymbol{\sigma}$ tends to Kirchhoff stress tensor $\boldsymbol{\tau}$ in practice. Consequently tensor $\boldsymbol{b}^{e-1}$ tends to the spatial metric tensor $\boldsymbol{g}$. In this case the distinction between intermediate and current configurations have no meaning. Then it is possible to write the elastic component of free energy function as a quadratic function of elastic component of Almansi strain tensor $\boldsymbol{e}^e$ and material constants λ and μ as can be seen in equation (39).

$$\psi^e = \left[\frac{1}{2} \lambda \; tr(\boldsymbol{e}^e)^2 \; + \; \mu \; (\boldsymbol{e}^e : \boldsymbol{e}^e) \right] \tag{39}$$

From equations (35) and (39) the Cauchy stress tensor results:

$$\sigma = \lambda \; tr(\boldsymbol{e}^e) \; \mathbf{1} \; + \; 2 \; \mu \; \boldsymbol{e}^e \tag{40}$$

This model has been used previously by the authors (García-Garino, 1993; García-Garino and Oliver, 1995, 1996) as an alternative to the neohookean models proposed by another authors (Simo, 1988a,b; Simo and Ortiz, 1985).

Plasticity is taken into account by means of an associative flow rule $f = g$. The yield function is the very well known Von Mises or J2 model given in equation (41).

$$f(\boldsymbol{\sigma}, \sigma_y) = \bar{\sigma} - \sigma_y = 0 \tag{41}$$

where $\bar{\sigma} = \sqrt{\frac{3}{2} \boldsymbol{s} : \boldsymbol{s}}$ denotes equivalent stress, $\boldsymbol{s}$ is the deviatoric stress tensor and σ_y is the current yield stress.

Flow rule can be written now in terms of yield criteria f:

$$\boldsymbol{d}^p = \dot{\gamma} \quad \boldsymbol{n} \qquad \text{where} \qquad \boldsymbol{n}_{ij} = \frac{\boldsymbol{s}_{ij}}{\sqrt{\boldsymbol{s}_{kl} \boldsymbol{s}_{kl}}} \tag{42}$$

where $(\boldsymbol{n} : \boldsymbol{n} = 1)$ is the unit outward normal to the yield surface and plastic multiplier γ can be computed plastic consistency condition.

The hardening law relates yield stress σ_y and the rate of the effective plastic strain $\dot{\bar{\epsilon}}^p$ defined as $\dot{\bar{\epsilon}}^p = \sqrt{\frac{2}{3} \; \boldsymbol{d}^p : \boldsymbol{d}^p}$ as shown in equation (43).

$$\dot{\sigma_y} \; = \; h \dot{\bar{\epsilon}}^p \; = \; \sqrt{\frac{2}{3}} \; h \; \dot{\gamma} \tag{43}$$

and h is a material parameter that corresponds to the slope of the effective stress vs. effective plastic strain curve under uniaxial loading conditions, also known as hardening module in the case of linear hardening.

3.2 Numerical implementation

In this section the numerical scheme necessary to implement the discussed theoretical model in a finite element code is derived following the ideas of Simo and Ortiz (1985); Simo (1988b). This scheme is based on a *elastic* predictor plus *plastic* corrector approach, derived in previous works of Garca Garino García-Garino (1993); García-Garino and Oliver (1996).

3.2.1 Elastic Problem

In this problem the plastic quantities remain frozen: $({}^{t+\Delta t}\boldsymbol{F}^{pTR} = {}^{t}\boldsymbol{F}^{p})$. The trial (*elastic*) component of the deformation gradient tensor results:

$$ {}^{t+\Delta t}\boldsymbol{F}^{eTR} = {}^{t+\Delta t}\boldsymbol{F} \ \left({}^{t+\Delta t}\boldsymbol{F}^{pTR}\right)^{-1} = \boldsymbol{f} \ {}^{t}\boldsymbol{F} \left({}^{t}\boldsymbol{F}^{p}\right)^{-1} = \boldsymbol{f} \ {}^{t}\boldsymbol{F}^{e} \tag{44} $$

where $\boldsymbol{f}$ is the incremental deformation gradient tensor. The predictor value of the elastic Finger tensor ${}^{t+\Delta t}\boldsymbol{b}^{e-1^{TR}}$ is:

$$ {}^{t+\Delta t}\boldsymbol{b}^{e-1^{TR}} = \left({}^{t+\Delta t}\boldsymbol{F}^{e-T} \ {}^{t+\Delta t}\boldsymbol{F}^{e-1} \right)^{TR} = \boldsymbol{f}^{-T} \ {}^{t}\boldsymbol{b}^{e-1} \ \boldsymbol{f}^{-1} \tag{45} $$

Finally, the trial stresses $\boldsymbol{\sigma}^{TR}$ are computed from eqn (45) in terms of the predictor value of elastic Almansi strain ${}^{t+\Delta t}\boldsymbol{e}^{eTR} = \frac{1}{2}({}^{t+\Delta t}\boldsymbol{g} \ - \ {}^{t+\Delta t}\boldsymbol{b}^{e-1^{TR}})$.

It is important to note that the elastic problem is reduced to the computation of a closed expression. In this way numerical integration of rate equations, typical of hypoelastic models and usually very expensives, is completely avoided. On the other hand it is not necessary to compute explicitely multiplicative decomposition of deformation gradient tensor $\boldsymbol{F}$.

3.2.2 Plastic Problem

In this problem the current configuration remains fixed and the internal variables are updated in order to satisfy the constitutive law. For this problem Simo (1988b) has proposed to integrate the flow rule in the original configuration:

$$ \dot{\boldsymbol{C}}^{p} = 2 \ \phi^{*}\boldsymbol{d}^{p} = 2 \ \dot{\lambda} \ \phi^{*}\boldsymbol{n} = 2 \ \dot{\lambda} \ \boldsymbol{N} \tag{46} $$

Equation (46) is integrated using a Backward-Euler scheme:

$$ {}^{t+\Delta t}\boldsymbol{C}^{p} - {}^{t}\boldsymbol{C}^{p} = 2 \, \lambda \, {}^{t+\Delta t}\boldsymbol{N} \tag{47} $$

where λ accounts for the numerical counterpart of plastic multiplier $\dot{\gamma}$. Pushing eq. (47) forward the spatial configuration, the updated Finger tensor is found:

$$ {}^{t+\Delta t}\boldsymbol{b}^{e-1} = {}^{t+\Delta t}\boldsymbol{b}^{e-1^{TR}} + 2 \, \lambda \, {}^{t+\Delta t}\boldsymbol{n} \tag{48} $$

The factor $2 \, \lambda \, {}^{t+\Delta t}\boldsymbol{n}$ is computed by means of the radial return algorithm.

4 VARIATIONAL FORMULATION OF FINITE PLASTICITY

4.1 Model formulation

Here, we recall the main features of the variational formulation of finite plasticity proposed by Ortiz and Stainier (1999).

The plastic deformation $\boldsymbol{F}^p$ is an internal variable, which represents the effect of permanent deformations in the crystal lattice. In Von Mises-type models of plasticity for polycrystalline materials, it is assumed that plastic flow does not generate any rotation or volume change in the material, which translates into a flow rule of the type:

$$\boldsymbol{L}^p = \dot{\bar{\epsilon}}^p \boldsymbol{M} \quad \text{with} \quad \boldsymbol{M} \in \text{Sym}, \boldsymbol{M} \cdot \boldsymbol{M} = \frac{3}{2}, \text{ and } \text{tr}[\boldsymbol{M}] = 0 \tag{49}$$

The direction of plastic flow is not specified further, since it will be determined by the variational principle described in the following. The internal variable $\bar{\epsilon}^p$ (cumulated plastic strain) will describe the hardening of the material.

We postulate the existence of a Helmholtz free energy density of the form

$$W(\boldsymbol{F}, \boldsymbol{F}^p, \bar{\epsilon}^p) = W^e(\boldsymbol{F}^e) + W^p(\boldsymbol{F}^p, \bar{\epsilon}^p) \tag{50}$$

From Objectivity conditions and uncoupled elasticity hypothesis, as has been discussed for the hyperelastic model, the free energy becomes:

$$W(\boldsymbol{F}, \boldsymbol{F}^p, \bar{\epsilon}^p) = W^e(\boldsymbol{C}^e) + W^p(\boldsymbol{F}^p, \bar{\epsilon}^p) \tag{51}$$

Physically, W^p represents the stored energy due to the plastic working of the material. The free energy density allows to define the forces thermodynamically conjugate to the state variables $\{\boldsymbol{F}, \boldsymbol{F}^p, \bar{\epsilon}^p\}$:

$$\boldsymbol{P} = \frac{\partial W}{\partial \boldsymbol{F}} = \boldsymbol{F}^e \left(2 \frac{\partial W^e}{\partial \boldsymbol{C}^e} \right) \tag{52}$$

$$\boldsymbol{T} = -\frac{\partial W}{\partial \boldsymbol{F}^p} = \boldsymbol{F}^{eT} \boldsymbol{P} - \frac{\partial W^p}{\partial \boldsymbol{F}^p} \tag{53}$$

$$Y = -\frac{\partial W}{\partial \bar{\epsilon}^p} = (\boldsymbol{T} \boldsymbol{F}^{pT}) \cdot \boldsymbol{M} - \frac{\partial W^p}{\partial \bar{\epsilon}^p} = (\boldsymbol{S} - \boldsymbol{S}^c) \cdot \boldsymbol{M} - \frac{\partial W^p}{\partial \bar{\epsilon}^p} \tag{54}$$

In deriving equation (54), we took into account the constraint between $\boldsymbol{F}^p$ and $\bar{\epsilon}^p$ arising from the flow rule (49). In this same equation, we observe the appearance of the Mandel stress tensor $\boldsymbol{S} = \boldsymbol{F}^{eT} \boldsymbol{P} \boldsymbol{F}^{pT}$ and its corresponding backstress $\boldsymbol{S}^c = \frac{\partial W^p}{\partial \boldsymbol{F}^p} \boldsymbol{F}^{pT}$.

In order to complete the model, we need to provide kinetic equations for the internal variables. Following a standard thermodynamic framework, we will consider a relation of the type:

$$\dot{\bar{\epsilon}}^p = f(Y; \bar{\epsilon}^p) \tag{55}$$

More precisely, we will assume that the kinetic relation derives from a convex dissipation pseudo-potential:

$$\dot{\bar{\epsilon}}^p = \frac{\partial \psi}{\partial Y}(Y; \bar{\epsilon}^p) \tag{56}$$

Convexity of $\psi(Y)$ then ensures the positiveness of internal dissipation: $\mathcal{D} = Y \dot{\bar{\epsilon}}^p \geq 0$. A dual pseudo-potential can be defined by recourse to a Legendre-Fenchel transform:

$$\psi^*(\dot{\bar{\epsilon}}^p; \bar{\epsilon}^p) = \sup_Y \left[Y \dot{\bar{\epsilon}}^p - \psi(Y; \bar{\epsilon}^p) \right] \tag{57}$$

with the property that

$$Y = \frac{\partial \psi^*}{\partial \dot{\bar{\epsilon}}^p}(\dot{\bar{\epsilon}}^p; \bar{\epsilon}^p) \tag{58}$$

Example: the case of rate-independent plasticity, which we will consider in the applications, can be derived from the following dissipation pseudo-potential:

$$\psi(Y) = \begin{cases} 0 & \text{if } Y \leq Y_0 \\ +\infty & \text{if } Y > Y_0 \end{cases} \tag{59}$$

where Y_0 is a material parameter corresponding to a yield stress. The dual potential is then given by:

$$\psi^*(\dot{\bar{\epsilon}}^p) = \begin{cases} Y_0\, \dot{\bar{\epsilon}}^p & \text{if } \dot{\bar{\epsilon}}^p \geq 0 \\ +\infty & \text{if } \dot{\bar{\epsilon}}^p < 0 \end{cases} \tag{60}$$

In this case, the dissipation pseudo-potentials are quasi-convex, but this does not pose any formal problems (Moreau, 1976; Rockafellar, 1970). □

As shown in Ortiz and Stainier (1999), the above constitutive relations can be recast in the form of a minimization problem. Consider the following functional:

$$D(\dot{\boldsymbol{F}}, \dot{\bar{\epsilon}}^p, \boldsymbol{M}; \boldsymbol{F}, \boldsymbol{F}^p, \bar{\epsilon}^p) \equiv \boldsymbol{P} \cdot \dot{\boldsymbol{F}} - Y\, \dot{\bar{\epsilon}}^p + \psi^*(\dot{\bar{\epsilon}}^p; \bar{\epsilon}^p) = \dot{W}(\boldsymbol{F}, \boldsymbol{F}^p, \bar{\epsilon}^p) + \psi^*(\dot{\bar{\epsilon}}^p; \bar{\epsilon}^p) \tag{61}$$

where $\boldsymbol{P}$ and Y are computed by relations (52) and (54). In the rate-independent case, this functional D corresponds to the power of external work, but this is not the case otherwise. Then the solutions to the minimization problem:

$$D^{\text{eff}}(\dot{\boldsymbol{F}}; \boldsymbol{F}, \boldsymbol{F}^p, \bar{\epsilon}^p) = \inf_{\boldsymbol{M}, \dot{\bar{\epsilon}}^p} D(\dot{\boldsymbol{F}}, \dot{\bar{\epsilon}}^p, \boldsymbol{M}; \boldsymbol{F}, \boldsymbol{F}^p, \bar{\epsilon}^p) \text{ with } \boldsymbol{M} \cdot \boldsymbol{M} = \frac{3}{2} \text{ and } \mathrm{tr}[\boldsymbol{M}] = 0 \tag{62}$$

verify the following relations:

$$\max_{\boldsymbol{M}} (Y\, \dot{\bar{\epsilon}}^p) \quad \text{with } \boldsymbol{M} \cdot \boldsymbol{M} = \frac{3}{2} \quad \text{and } \mathrm{tr}[\boldsymbol{M}] = 0 \tag{63}$$

$$-Y + \frac{\partial \psi^*}{\partial \dot{\bar{\epsilon}}^p} = 0 \tag{64}$$

Relation (63) states the principle of maximum plastic dissipation (Lubliner, 1990). In this case, the solution can be obtained analytically, and yields:

$$\boldsymbol{M} = \sqrt{\frac{3}{2}} \frac{\mathrm{dev}[\boldsymbol{S} - \boldsymbol{S}^c]}{\|\mathrm{dev}[\boldsymbol{S} - \boldsymbol{S}^c]\|} \tag{65}$$

This corresponds to the normality rule of classical Von Mises theory of plasticity (expressed in the intermediate configuration). Relation (64) is obviously identical to (58).

In addition, we have the following property:

$$\boldsymbol{P} = \frac{\partial D^{\text{eff}}}{\partial \dot{\boldsymbol{F}}}(\dot{\boldsymbol{F}}; \boldsymbol{F}, \boldsymbol{F}^p, \bar{\epsilon}^p) \tag{66}$$

showing that the functional D^{eff} plays the role of a rate-potential for stresses. The significance of this property will appear more clearly in the framework of incremental constitutive updates.

4.2 Constitutive updates

In the incremental setting, we are concerned with the following problem. Consider a generic time interval $[t_n, t_{n+1}]$. Let the initial state $\{\boldsymbol{F}_n, \boldsymbol{F}^p_n, \bar{\epsilon}^p_n\}$ and the updated deformations $\boldsymbol{F}_{n+1}$ be given. We then seek to compute updated values for the internal variables $\{\boldsymbol{F}^p_{n+1}, \bar{\epsilon}^p_{n+1}\}$.

The first step in effecting an integration of the constitutive relations is to provide an incremental rule to update $\boldsymbol{F}^p$ in a manner compatible with the flow rule (49). We take this rule to be of the form:

$$\boldsymbol{F}^p_{n+1} = \exp[\Delta\bar{\epsilon}^p \boldsymbol{M}]\boldsymbol{F}^p_n \tag{67}$$

where $\exp[\bullet]$ is the exponential mapping operator for symmetric square tensors and $\Delta\bar{\epsilon}^p = \bar{\epsilon}^p_{n+1} - \bar{\epsilon}^p_n$. The exponential mapping has been applied to the integration of finite-deformation flow rules by Weber and Anand (1990), Eterovic and Bathe (1990), Cuitiño and Ortiz (1992), Miehe and Stein (1992) and Miehe (1996). A particularly appealing aspect of the exponential mapping is that it satisfies exactly the finite-deformation extension of kinematic constraints operating on $\boldsymbol{M}$. For instance, since $\boldsymbol{M}$ is traceless, in keeping with plastic incompressibility, the plastic deformation $\boldsymbol{F}^p_{n+1}$ computed through (67) has a determinant of one, as required.

A variational constitutive update algorithm can be modelled after the rate variational principle (62). To this end, we define the incremental energy density:

$$\begin{aligned}\mathcal{W}(\boldsymbol{F}_{n+1}; \boldsymbol{F}_n, \boldsymbol{F}^p_n, \bar{\epsilon}^p_n) \equiv \\ \inf_{\bar{\epsilon}^p_{n+1}, \boldsymbol{M}} \left[W(\boldsymbol{F}_{n+1}, \boldsymbol{F}^p_{n+1}, \bar{\epsilon}^p_{n+1}) - W(\boldsymbol{F}_n, \boldsymbol{F}^p_n, \bar{\epsilon}^p_n) + \Delta t\ \psi^*\left(\frac{\Delta\bar{\epsilon}^p}{\Delta t}; \bar{\epsilon}^p_{n+\alpha}\right)\right] \\ \text{with } \boldsymbol{M}\cdot\boldsymbol{M} = \frac{3}{2} \text{ and } \mathrm{tr}[\boldsymbol{M}] = 0\end{aligned} \tag{68}$$

where $\bar{\epsilon}^p_{n+\alpha} = (1-\alpha)\bar{\epsilon}^p_n + \alpha\bar{\epsilon}^p_{n+1}$ is function of the algorithmic parameter $\alpha \in [0,1]$. Evidently, the choice of incremental energy density $\mathcal{W}$ is not unique. The particular form (68) adopted above is motivated by the midpoint rule for numerical integration. The stationarity condition with respect to $\bar{\epsilon}^p_{n+1}$ yields

$$\frac{\partial W}{\partial \bar{\epsilon}^p}(\boldsymbol{F}_{n+1}, \boldsymbol{F}^p_{n+1}, \bar{\epsilon}^p_{n+1}) + \frac{\partial \psi^*}{\partial \dot{\bar{\epsilon}}^p}\left(\frac{\Delta\bar{\epsilon}^p}{\Delta t}; \bar{\epsilon}^p_{n+\alpha}\right) = -Y_{n+1} + \frac{\partial \psi^*}{\partial \dot{\bar{\epsilon}}^p}\left(\frac{\Delta\bar{\epsilon}^p}{\Delta t}; \bar{\epsilon}^p_{n+\alpha}\right) = 0 \tag{69}$$

which is an incremental version of the kinetic relation (58). The stationarity condition with respect to $\boldsymbol{M}$ yields an incremental version of the principle of maximum plastic dissipation (63).

In the examples below, we will consider an elastic free energy density of the specific form:

$$W^e(\boldsymbol{C}^e) = f(J^e) + \mu\|\boldsymbol{e}^e\|^2 \quad \text{with } \boldsymbol{e}^e = \mathrm{dev}[\boldsymbol{\epsilon}^e] \text{ and } \boldsymbol{\epsilon}^e = \log[\sqrt{\boldsymbol{C}^e}] = \tfrac{1}{2}\log[\boldsymbol{C}^e] \tag{70}$$

where μ is the shear modulus and $J^e = \det \boldsymbol{F}^e = \sqrt{\det \boldsymbol{C}^e}$ is the elastic Jacobian. Using (67), we can write

$$\begin{aligned}\boldsymbol{C}^e_{n+1} &= \exp[\Delta\bar{\epsilon}^p\boldsymbol{M}]^{-T}\boldsymbol{F}^{p\,-T}_n\boldsymbol{C}_{n+1}\boldsymbol{F}^{p\,-1}_n\exp[\Delta\bar{\epsilon}^p\boldsymbol{M}]^{-1} \\ &= \exp[\Delta\bar{\epsilon}^p\boldsymbol{M}]^{-T}\boldsymbol{C}^{e,\mathrm{pr}}_{n+1}\exp[\Delta\bar{\epsilon}^p\boldsymbol{M}]^{-1}\end{aligned} \tag{71}$$

where we introduced a predictor elastic right Cauchy-Green deformation $\boldsymbol{C}^{e,\mathrm{pr}}_{n+1}$, i.e. the elastic deformation which would be obtained at the end of the step if the increment were entirely elastic ($\Delta\bar{\epsilon}^p = 0$). Using the *ansatz* that $\boldsymbol{C}^{e,\mathrm{pr}}_{n+1}$ and $\boldsymbol{M}$ share the same eigenvectors, we then can write

$$\boldsymbol{\epsilon}^e_{n+1} = \tfrac{1}{2}\log[\boldsymbol{C}^{e,\mathrm{pr}}_{n+1}] - \Delta\bar{\epsilon}^p\boldsymbol{M} = \boldsymbol{\epsilon}^{e,\mathrm{pr}}_{n+1} - \Delta\bar{\epsilon}^p\boldsymbol{M} \tag{72}$$

In the case of the above elastic potential (70), and assuming that the plastic potential does not explicitely depend on $\boldsymbol{F}^p$ (isotropic hardening), the minimization with respect to $\boldsymbol{M}$ then reduces to

$$\inf_{\boldsymbol{M}} \left[\mu \|\boldsymbol{e}^{e,\mathrm{pr}}_{n+1} - \Delta\bar{\epsilon}^p \boldsymbol{M}\|^2\right] \quad \text{with } \boldsymbol{M}\cdot\boldsymbol{M} = \frac{3}{2} \text{ and } \mathrm{tr}[\boldsymbol{M}] = 0 \tag{73}$$

The solution may readily be obtained by recourse to Lagrange multipliers, yielding:

$$\boldsymbol{M} = \sqrt{\frac{3}{2}} \frac{\boldsymbol{e}^{e,\mathrm{pr}}_{n+1}}{\|\boldsymbol{e}^{e,\mathrm{pr}}_{n+1}\|} \tag{74}$$

Once the optimal direction of plastic flow for the step has been determined, the increment in effective plastic strain follows from the problem:

$$\inf_{\bar{\epsilon}^p_{n+1}} \left[\mu \|\boldsymbol{e}^{e,\mathrm{pr}}_{n+1} - \Delta\bar{\epsilon}^p \boldsymbol{M}\|^2 + W^p(\bar{\epsilon}^p_{n+1}) + \Delta t \psi^* \left(\frac{\Delta\bar{\epsilon}^p}{\Delta t}\right)\right] \tag{75}$$

Note that $\Delta\bar{\epsilon}^p$ must satisfy the constraint $\Delta\bar{\epsilon}^p \geq 0$ by virtue of (60). The value $\Delta\bar{\epsilon}^p = 0$, which corresponds to an elastic step, defines a non-smooth point of the objective function (75). A conventional mean of sidestepping this difficulty is to first investigate the solution $\Delta\bar{\epsilon}^p = 0$, which corresponds to a purely elastic update, or elastic predictor. If the attendant driving force $Y - Y_0 > 0$ then one must have $\Delta\bar{\epsilon}^p > 0$ instead, and the solid is loaded plastically. Since the function (75) of $\Delta\bar{\epsilon}^p$ is smooth away from the origin, the case of plastic loading may be solved, e.g. by a local Newton-Raphson iteration, by finding the root of

$$\bar{\sigma}(\Delta\bar{\epsilon}^p) - \kappa(\bar{\epsilon}^p_{n+1}) - Y_0 = 0 \tag{76}$$

where

$$\bar{\sigma} = \sqrt{\frac{3}{2}} \left(2\mu \|\boldsymbol{e}^{e,\mathrm{pr}}_{n+1} - \Delta\bar{\epsilon}^p \boldsymbol{M}\|\right) \tag{77}$$

is the equivalent stress in the intermediate configuration and $\kappa(\bar{\epsilon}^p_{n+1}) = \partial W^p / \partial \bar{\epsilon}^p$ is an additional contribution to the yield stress. In the particular case of the elastic potential (70), the variational update is thus mostly equivalent to the traditional radial return algorithm.

Imagine now perturbing $\boldsymbol{F}_{n+1} \to \boldsymbol{F}_{n+1} + \delta\boldsymbol{F}$. The corresponding variation of $\mathcal{W}$ is

$$\delta\mathcal{W} = \frac{\partial W}{\partial \boldsymbol{F}}(\boldsymbol{F}_{n+1}, \boldsymbol{F}^p_{n+1}, \bar{\epsilon}^p_{n+1}) \cdot \delta\boldsymbol{F} + \frac{\partial \mathcal{W}}{\partial \bar{\epsilon}^p_{n+1}} \cdot \delta\bar{\epsilon}^p_{n+1} + \frac{\partial \mathcal{W}}{\partial \boldsymbol{M}} \cdot \delta\boldsymbol{M} \tag{78}$$

But the last two terms vanish by virtue of the stationarity condition of $\mathcal{W}$ with respect to $\{\bar{\epsilon}^p_{n+1}, \boldsymbol{M}\}$, and (78) reduces to

$$\delta\mathcal{W} = \boldsymbol{P}_{n+1} \cdot \delta\boldsymbol{F} \tag{79}$$

Since $\delta\boldsymbol{F}$ is arbitrary, this implies that

$$\boldsymbol{P}_{n+1} = \frac{\partial \mathcal{W}}{\partial \boldsymbol{F}_{n+1}}(\boldsymbol{F}_{n+1}; \boldsymbol{F}_n, \boldsymbol{F}^p_n, \bar{\epsilon}^p_n) \tag{80}$$

Equation (80) furnished a stress update, and in addition, we observe that $\mathcal{W}$ acts as a pseudo-hyperelastic potential for $\boldsymbol{P}_{n+1}$.

5 NECKING OF A CYLINDRICAL BAR

5.1 Numerical model

The numerical simulation of necking in a cylindrical bar in tension, see García-Garino et al. (2006, 2004) and references therein is the first benchmark studied in this work . The model used here reproduces the sample used in experimental tests by Goicolea (1985). The bar is 75 mm long and has a diameter of 16.2 mm. The numerical model only considers one half of the bar and uses the axial symmetry, resulting in the finite element meshes shown in Figure 2. In all meshes, a small imperfection is introduced in the central section, where the radius is reduced by 1.8518%. The radius varies linearly between the extremity and the central section. Stress distribution at necking section, previously discussed in the cited works of García-Garino et al. (2006, 2004) as well as load histories like discussed by Ponthot (1995); Simo (1988b) are analysed here.

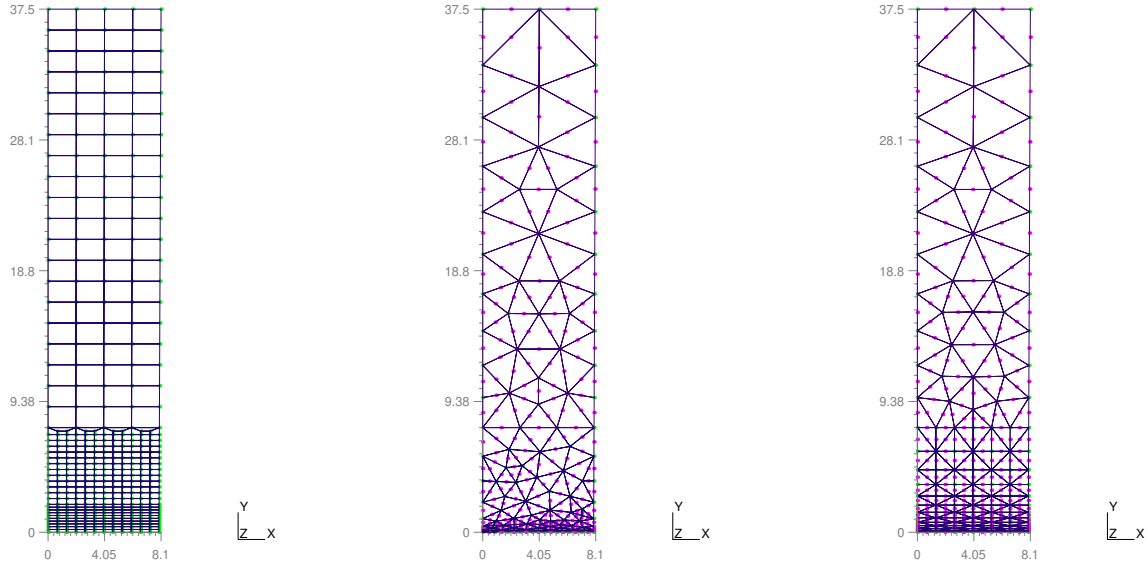

(a) quadrangles [Q1] (b) unstructured triangles [T2a] (c) structured triangles [T2b]

Figure 2: Finite element meshes of the bar

In the following we will compare the results obtained with bilinear quadrangles (and the mixed formulation briefly presented in the previous section), using the mesh in Fig. 1(a), and with quadratic triangles (and a standard isoparametric formulation). We used two triangular meshes: a first one, Fig. 1(b), completely unstructured, and a second one, Fig. 1(c), with a regular arrangement of triangles in the central zone, and labelled as structured. All meshes are refined in the zone where necking will occur. For information, the characteristics of all three meshes are summarized in Table 1. Note that all meshes roughly present the same number of nodes (leading to systems with similar number of unknowns), but that triangular meshes, with quadratic elements, present about half the number of elements compared to the quadratic mesh.

The material is an aluminium, with the following elastic properties:

$$E = 67000 \text{ MPa} \quad \nu = 0.3$$

while the hardening law is given by

$$Y(\bar{\epsilon}^p) = A(b + \bar{\epsilon}^p)^n = Y_0(1 + H\bar{\epsilon}^p)^n \tag{81}$$

Table 1: Summary of mesh characteristics

Mesh	Q1	T2a	T2b
# nodes	412	396	465
# elements	419	203	236

with $A = 181.7$ MPa, $n = 0.159$ and $b = 2.989\,10^{-4}$ (such that $Y_0 = 50$ MPa) (Goicolea, 1985).

5.2 Results

The tensile test consists in elongating the bar by 10 mm at each extremities. Because of the defect, an instability appears, and the bar starts necking. The deformed geometries obtained with both the quadrangular and the structured triangular meshes, as well as the related distributions of plastic strain, are shown on Figure 3.

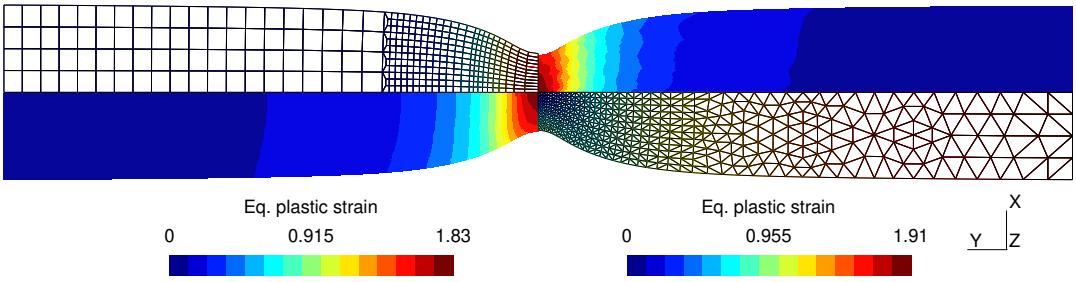

Figure 3: Final deformed geometries and equivalent plastic strain distributions for Q1 and T2b meshes

In order to compare a little more precisely the different formulations, we will start by looking at macroscopic quantities. Figure 4 shows the reduction of radius in the central section in function of elongation. Curves obtained with the fully variational formulation of quadrangles (ZorgLib Q1/P0) and with the standard formulation of quadratic triangles (ZorgLib T2a/b) compare rather well both with the solutions obtained by SOGDE and with a reference solution obtained in Abaqus. Note that the necking appears slightly less pronounced with SOGDE, a result which will be confirmed by further comparison. Next, Figure 5 compares the tensile force as a function of the logarithmic strain in the neck. Indeed, from the incompressibility of the plastic flow, and neglecting the elastic deformations in the neck zone, the diameter D can be linked to the logarithmic strain in the neck $\bar{\epsilon}_z$:

$$\bar{\epsilon}_z = -2 \log \frac{D}{D_0} \tag{82}$$

Finally, Figure 6 shows the average axial stress in the neck as a function of the same logarithmic strain. In both cases, all formulations considered here coincide, which show that they reproduce the same macroscopic tensile behaviour, the only difference being in the prediction of the onset of the necking instability. In other words, the stress-strain path in the necking zone seems to be unique, which can be explained by the theoretical developments of Bridgman (1964). But the different models end up at different locations on this path for a given elongation

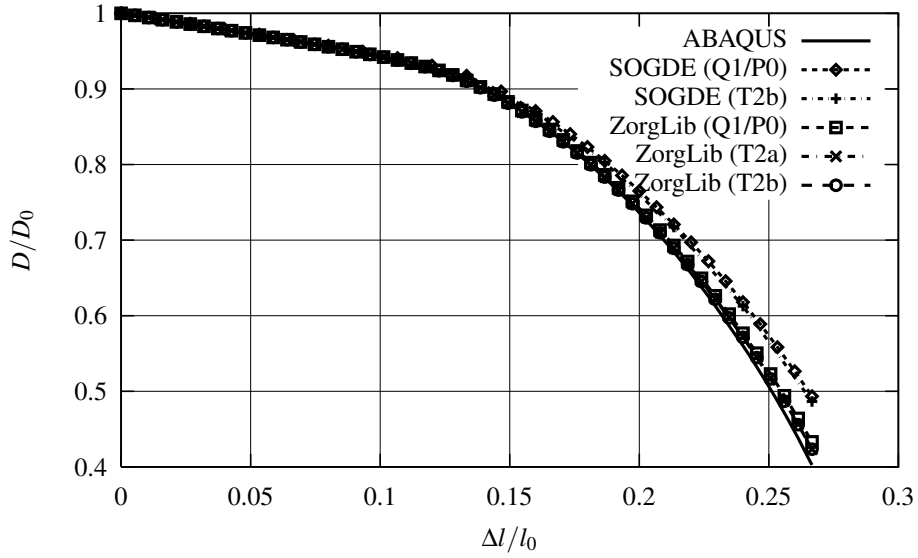

Figure 4: Diameter reduction in central section as a function of elongation

(at least in the post-critical part, after the onset of the necking instability). This results agree very well with the ones reported in García-Garino et al. (2004) .

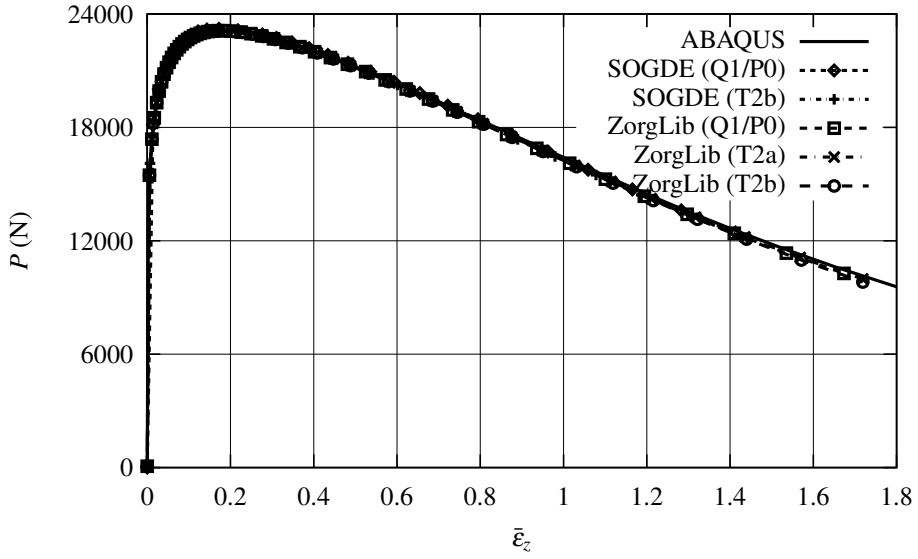

Figure 5: Tensile force as a function of logarithmic strain in the neck

These results show that neither the constitutive formulation (variational total Langrangean hyperelastic formulation of ZorgLib, updated Lagrangean hyperelastic formulation of SOGDE, or hypoelastic formulation of Abaqus), nor the finite element formulation (mixed formulation with bilinear quadrangles or standard formulation with quadratic triangles) leads to significant differences in terms of macroscopic quantities. At this global level, all formulations appear equally valid.

5.3 Stress distribution in the neck

In order to compare the different formulations a little deeper, it is interesting to look at local quantities. For example, one can get a qualitative comparison by examining maps of

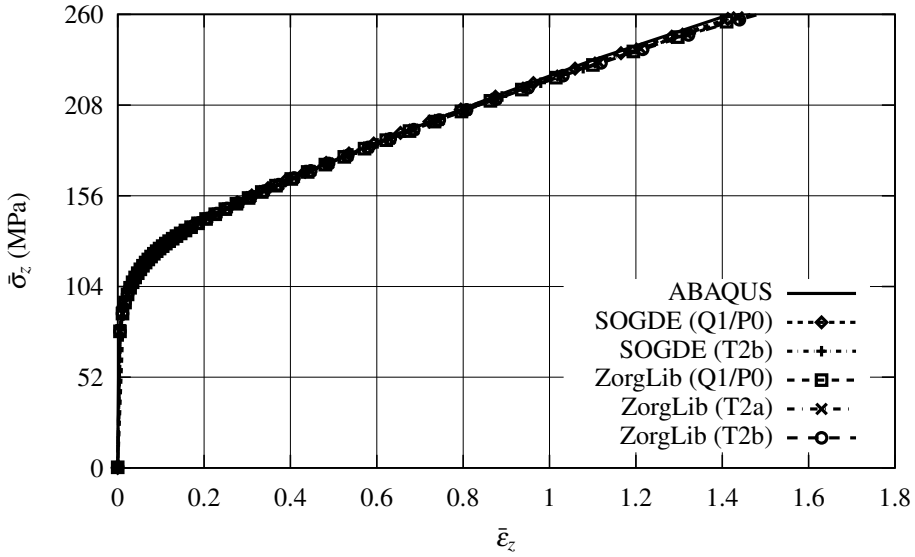

Figure 6: Axial stress as a function of logarithmic strain in the neck

equivalent plastic strain at the end of the simulation, as in Figure 3, or in the necking zone (which is of most interest), as in Figure 7. Note that in this last figure, the 6-noded quadratic triangles have been subdivided in four 3-noded triangles for the purpose of representation. We can readily observe that the more regular quadrangular mesh yields a smoother strain field than the triangular meshes, but this is also in large part a post-processing effect. On the other hand, the triangular meshes, and more specially the structured mesh T2b, perform better at representing the curvature at the neck. Thus, in the necking regime, the quadrangular mesh appears somewhat stiffer than the triangular meshes, which is also translated in the maximal value of plastic strain reached at that point.

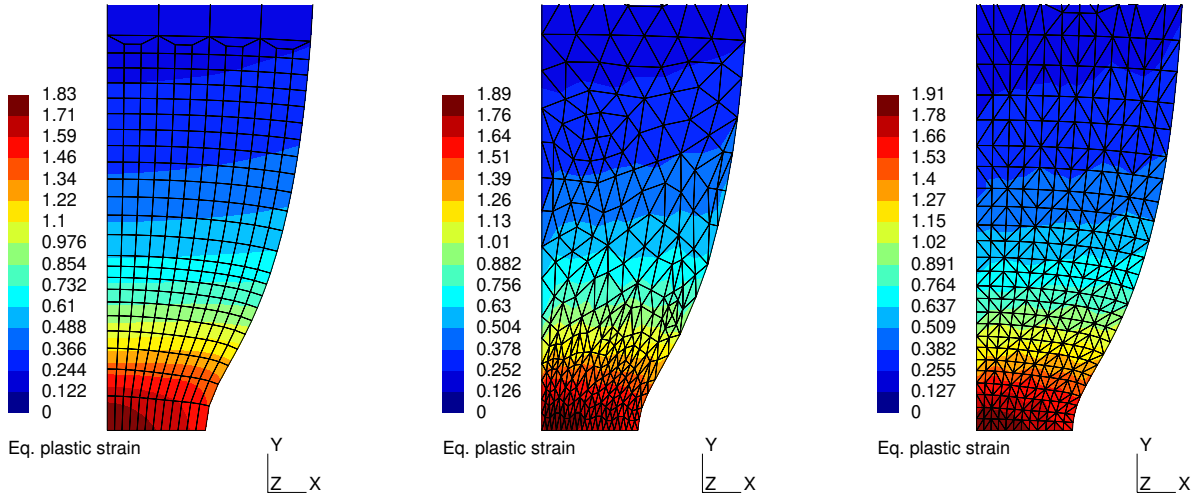

(a) Q1: quadrangles (b) T2a: unstructured triangles (c) T2b: structured triangles

Figure 7: Details of equivalent plastic strain distribution in neck

In order to get a more quantitative comparison of stress distribution in the neck, we can go back to the analytical theory of Bridgman (1964). Considerations on the strain state in the neck

yield that the stress state must be of the form:

$$\boldsymbol{\sigma} = \begin{pmatrix} \sigma_r & 0 & 0 \\ 0 & \sigma_r & 0 \\ 0 & 0 & \sigma_z \end{pmatrix} \tag{83}$$

where the stress components are expressed in the axisymmetric coordinate system. Von Mises yield criterion then becomes:

$$\sigma_z - \sigma_r = Y \tag{84}$$

Further analytical developments (Bridgman, 1964) lead to the following expression for the axial stress in the neck:

$$\sigma_z = Y \left[1 + \log \left(1 - \frac{r^2}{DR} + \frac{D}{4R} \right) \right] \tag{85}$$

where D is the bar diameter at the neck, R the curvature radius of the neck, and r the radial distance from the symmetry axis (the index z here corresponds to the axial direction in the axisymmetric coordinate system r, θ, z). The diameter D can easily be measured from the computations, but it is more difficult to obtain an expression for the curvature radius R, or even to measure it precisely from the computational results. Bridgman (1964) proposed the following expression:

$$\frac{D}{R} = 2\sqrt{\bar{\epsilon}_z - 0.1} \qquad (\bar{\epsilon}_z > 0.1) \tag{86}$$

Alternatively, the radius R can be measured directly from the computational results, by fitting a circular arc through two boundary nodes (see Fig. 8). A certain level of uncertainty is associated to this method, though, since the choice of the two nodes can lead to significant differences in the value of the computed radius (especially in the case of quadratic triangles, where one can hesitate between a mid-node and a vertex). This is nonetheless the option we will take, with the results listed in Table 2. The first node considered is of course the boundary node located on the longitudinal symmetry axis. The circle must pass through this node and we also know that its center must lie on this symmetry axis. For the quadrangular mesh, the second node through which the circle must pass is taken as the next node on the boundary, sharing the same element with the first one. In the case of the triangular mesh, we considered two possibilities for the second node: either it is the mid-node on the boundary edge, either it is the other vertex of this edge (Fig. 8 shows the first option). In any case, the position of this second node completely defines the circle from which we measure the curvature radius.

The numerical simulation of stress distribution at necking zone shown slight discrepancies with results due to Bridgman (1964), as was reported in García-Garino et al. (2006). In order to clarify this point Gabaldón (1999) suggested to compare distribution of deviatoric component of stress tensor as well as pressure at necking zone. A very good agreement for deviatoric components but discrepancies for pressure distribution were found (García-Garino et al., 2004). There is no clear explanation available for this point, and the finite element approximation used was one of the possible cause addressed. This result suggests to review the deviatoric components and pressure distributions in this work. In order to do that, analytical distributions are derived. Accounting for (84), the hydrostatic stress (pressure) is given by

$$p = \frac{2\sigma_r + \sigma_z}{3} = \sigma_z - \frac{2}{3}Y \tag{87}$$

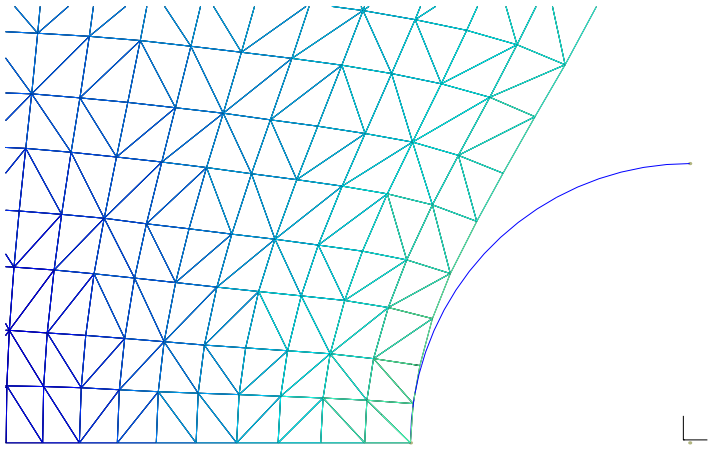

Figure 8: Numerical measure of the curvature radius in the neck (with a mid-node in this case)

Table 2: Measured curvature radius and neck diameter for successive elongations

	ZorgLib (Q1/P0)			ZorgLib (T2b)			
Δl [mm]	R	$D/2$	$\bar{\epsilon}_z$	$R^{(1)}$	$R^{(2)}$	$D/2$	$\bar{\epsilon}_z$
6.0	27.743	6.8320	0.303	21.356	12.417	6.8152	0.308
7.0	19.356	6.2511	0.481	14.053	9.224	6.2279	0.488
8.0	10.559	5.5088	0.734	7.349	5.264	5.4788	0.745
9.0	5.351	5.5860	1.100	3.997	3.097	4.5431	1.119
10.0	2.833	3.4433	1.673	2.272	1.974	3.3659	1.719

(1) radius measured with first boundary vertex
(2) radius measured with first boundary mid-node

and thus, using (85), we can write

$$\frac{p}{Y} = \frac{1}{3} + \log\left(1 - \frac{r^2}{DR} + \frac{D}{4R}\right) \tag{88}$$

while the deviatoric stress components are

$$s_r = -\frac{1}{3}Y \tag{89}$$

$$s_r = \frac{2}{3}Y \tag{90}$$

It is important to note that while s_r and s_r are constants, pressure distribution depends on the curvature radius in the neck, a variable that it is difficult to model. In this sense it is important to point that Bridgman proposed a function for r based on various simplificative assumptions. The resulting distributions are illustrated in the following figures, for the various meshes and at successive loading steps. In all cases, the agreement is excellent for deviatoric stresses. In the case of the quadrangular mesh (Fig. 9), there is a difference in the pressure distribution, more marked as the loading level increases. But it should be noted that this discrepancy comes not from the shape of the distribution, but from the value of the curvature radius (by playing with this value, the numerical distribution can be made to fit the theoretical one). Thus, the observed

difference hints at the fact that the computation of the curvature radius from nodal positions is not really precise.

In the case of triangular meshes (Fig. 10 and Fig. 11), the correspondence is better, except in the case of the unstructured mesh, where the high level of element distortion at high loading levels leads to a very scattered distribution of pressure, clearly unphysical. This scattering effect is much lessened by the use of the structured mesh, but would probably still show up at higher elongations. So, on the one hand, the structured triangular mesh seems to provide a better approximation of the curvature radius (values obtained with the mid-point node were used), but on the other hand, the distortion of the mesh at high loading levels could be considered as a limitation to the use of triangular quadratic elements.

Finally it is worthwhile to remark that pressure distribution results in the necking zone exhibit discrepancies for the formulations and finite element approximations considered in this work. Results obtained with quadratic triangular elements, based in displacements, suggests that perhaps the lack of agreement in pressure distribution is due to difficulties in properly computing the curvature radius at the neck zone and does not come from the finite element approaches. Further discussions on these results will be addressed.

6 GRECO BEAM BENDING

6.1 Numerical model

In order to further compare the different formulations, we now consider a classical benchmark, initially proposed within the research group "GRECO Grandes déformations et endommagement" in the 80's. It consists of a beam (length 3mm, thickness 1mm), as illustrated in Figure 12, in plane strain state, clamped at its left side and to which a large displacement (of 1mm downwards) is imposed on its upper right corner.

Different meshes were considered, based on 4-noded (bilinear) quadrangles and 6-noded (quadratic) triangles. All meshes share the same number (and initial position) of nodes. Like in the previous example, triangular meshes have half the number of elements of the quadrangular mesh.

The material of the beam is steel-like, with the following elastic properties:

$$E = 200000\,\text{MPa} \quad \nu = 0.3$$

while the hardening law is linear:

$$Y(\bar{\epsilon}^p) = \sigma_y^0 + H\bar{\epsilon}^p \tag{91}$$

with $\sigma_y^0 = 400$ MPa and $H = 1000$ MPa.

6.2 Results

Contours of equivalent plastic strain in the fully deformed beam are illustrated in Figure 13, for the various meshes, used with the fully variational formulation of ZorgLib. Again, for the purpose of the representation, quadratic triangles have been subdivided in linear triangles on these plots. Few differences appear on the deformed shape, except maybe for a more marked fold on the lower left corner in the case of the quadrangular mesh. As for the plastic strain distribution, it looks like the quadrangular mesh yields better results, since the maxima are well located on the outer fibres, as should be in pure bending. Triangular meshes yield less regular distributions.

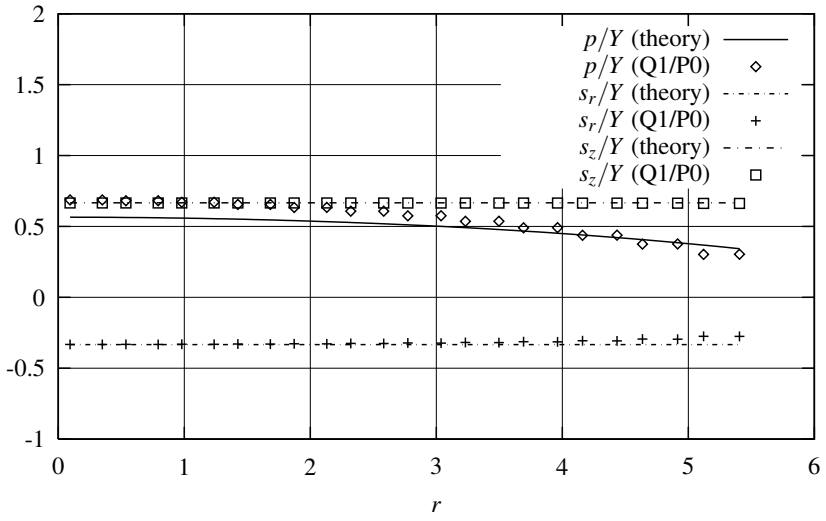

(a) $\Delta l = 8$ mm

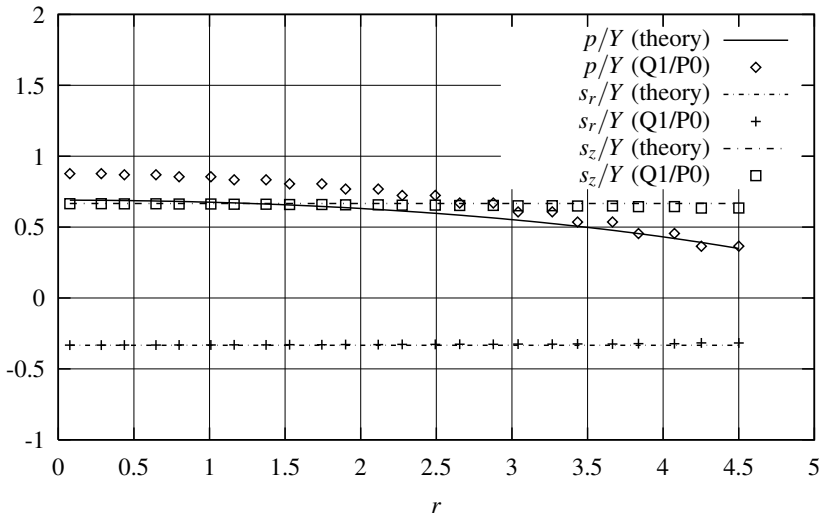

(b) $\Delta l = 9$ mm

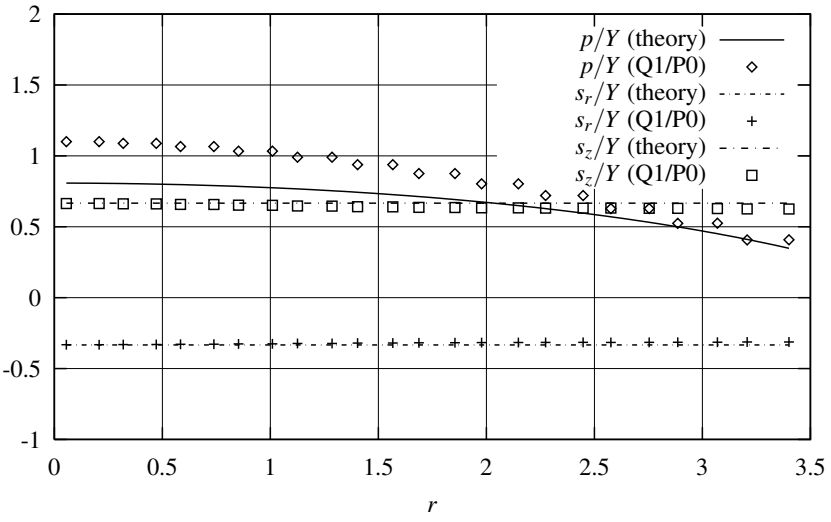

(c) $\Delta l = 10$ mm

Figure 9: Radial distribution of stresses in neck (ZorgLib Q1/P0)

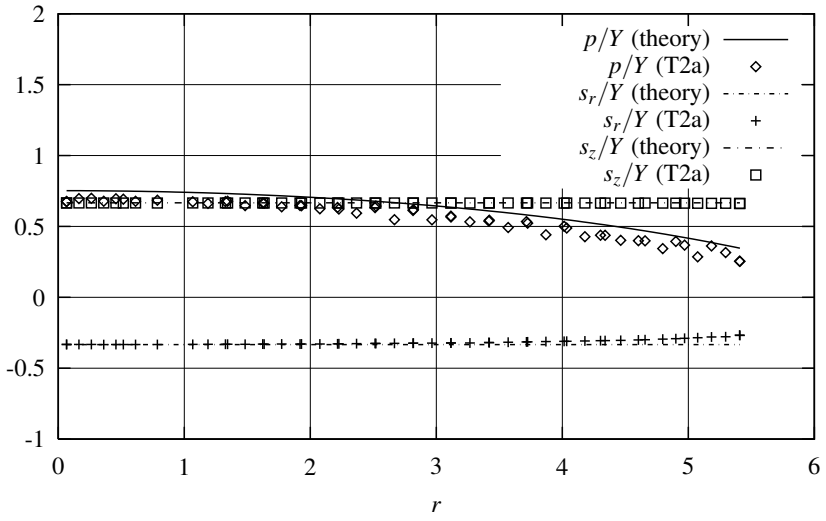

(a) $\Delta l = 8$ mm

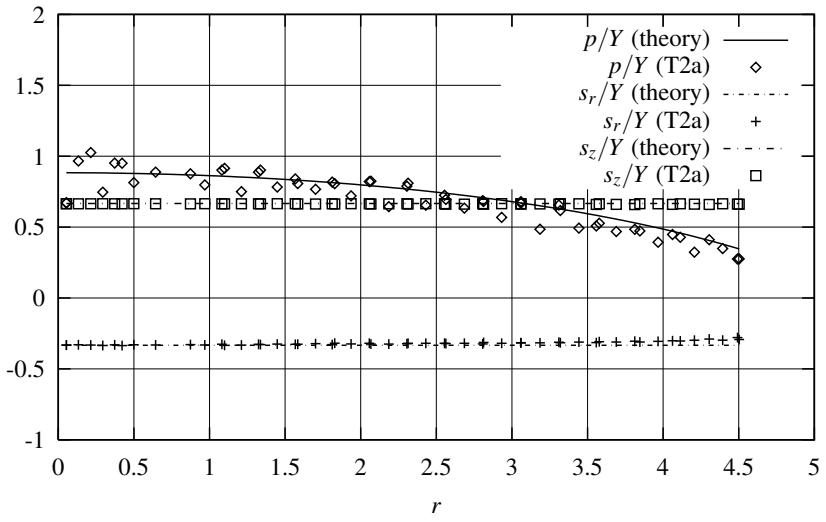

(b) $\Delta l = 9$ mm

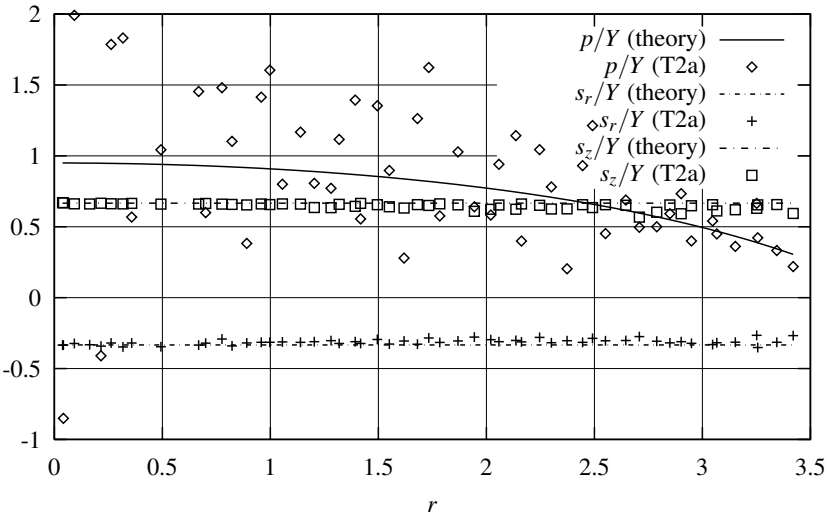

(c) $\Delta l = 10$ mm

Figure 10: Radial distribution of stresses in neck (ZorgLib T2a)

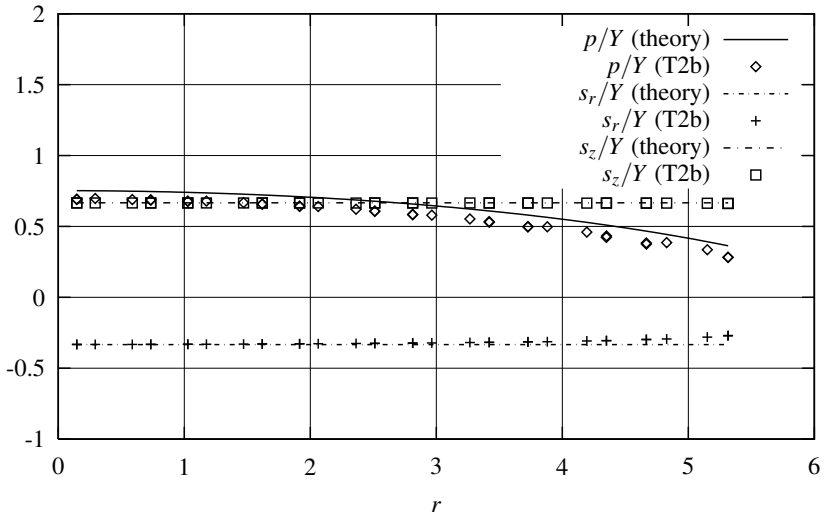

(a) $\Delta l = 8$ mm

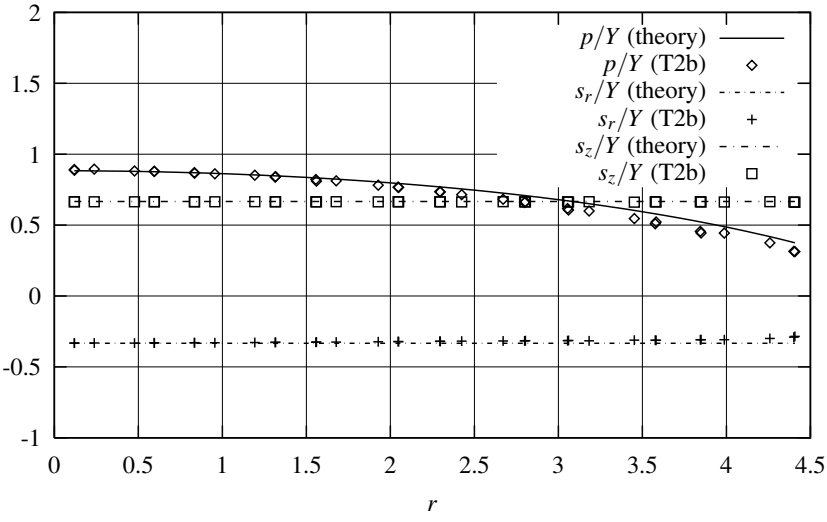

(b) $\Delta l = 9$ mm

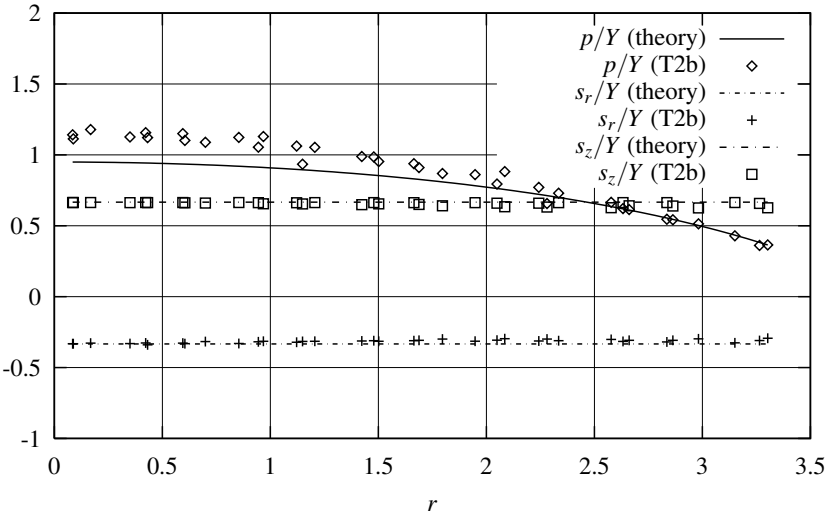

(c) $\Delta l = 10$ mm

Figure 11: Radial distribution of stresses in neck (ZorgLib T2b)

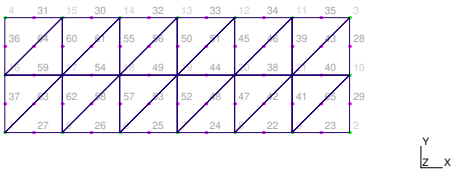

(triangles left)

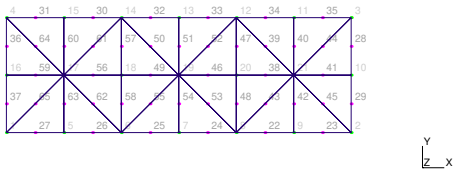

(triangles crossed)

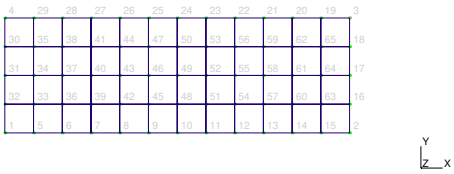

(quadrangles)

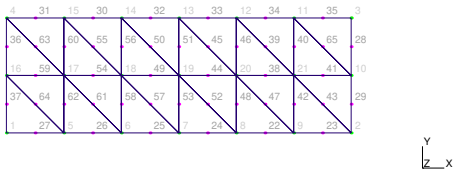

(triangles right)

Figure 12: Meshes for the GRECO beam

In terms of macroscopic quantities, we can compare results from ZorgLib to those of SOGDE. Figure 14 shows the different force-displacement curves. The agreement between ZorgLib and SOGDE is very good, despite differences in the formulation of the elastoplastic constitutive update, and in the formulation of the quadrangular element. It is interesting to note that the crossed triangles curve follows the quadrangles curve in the first half of the loading path, and then transitions to the left triangles in the second half. In the same manner, the right triangles transitions to the quadrangles curve at higher levels of loading.

A more detailed analysis, comparing stress components in integration points seems necessary and it will be performed in the future steps of this collaboration.

7 CYLINDER UPSETTING

7.1 Numerical model

The last application concerns the upsetting of a cylindrical billet (of radius 6 and half-height 1.5). Given both axial and longitudinal symmetries, only the upper part of the specimen is modelled in an axisymmetrical setting. As before, different meshes, based on 4-noded quadrangles and 6-noded triangles, will be considered (Fig. 15).

As it was the case with the GRECO beam, all meshes share the same number of nodes (and identical nodal positions), while triangular meshes have half the number of elements of the quadrangular mesh.

The billet is made of a model material, with the following elastic properties:

$$E = 1000 \quad \nu = 0.3$$

while the hardening law is linear (91) with

$$\sigma_y^0 = 1 \quad H = 3$$

7.2 Results

The upsetting process is simulated by applying an imposed displacement to the upper face of the billet. This imposed displacement is purely vertical (no horizontal sliding allowed) and leads

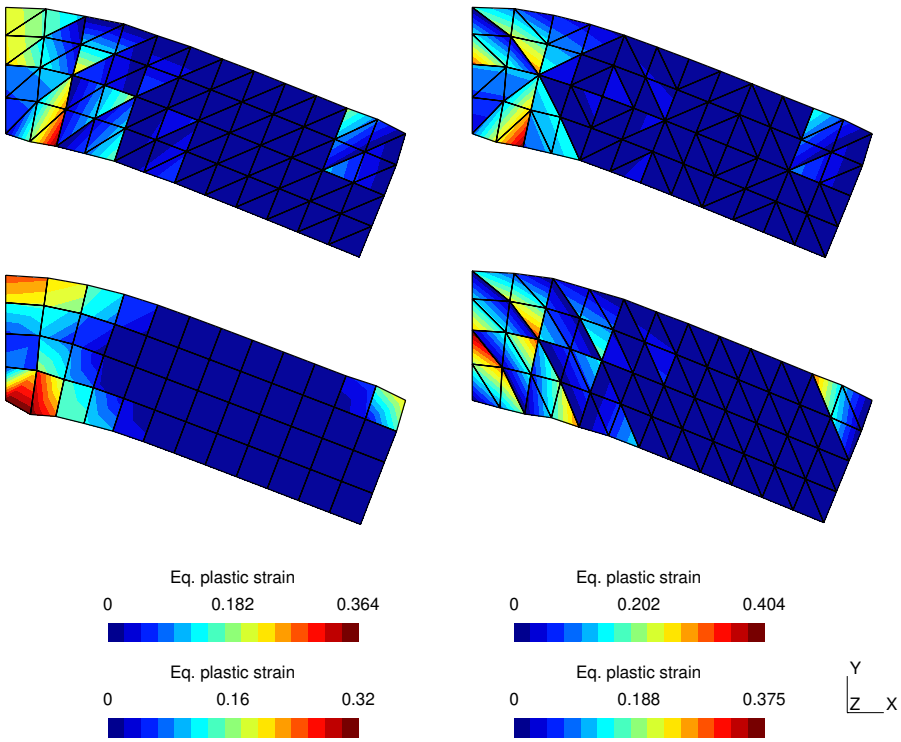

Figure 13: Distribution of plastic strain for various meshes (from left to right, bottom to top: quadrangles, triangles right, triangles left, triangles crossed). All results obtained with the fully variationnal formulation.

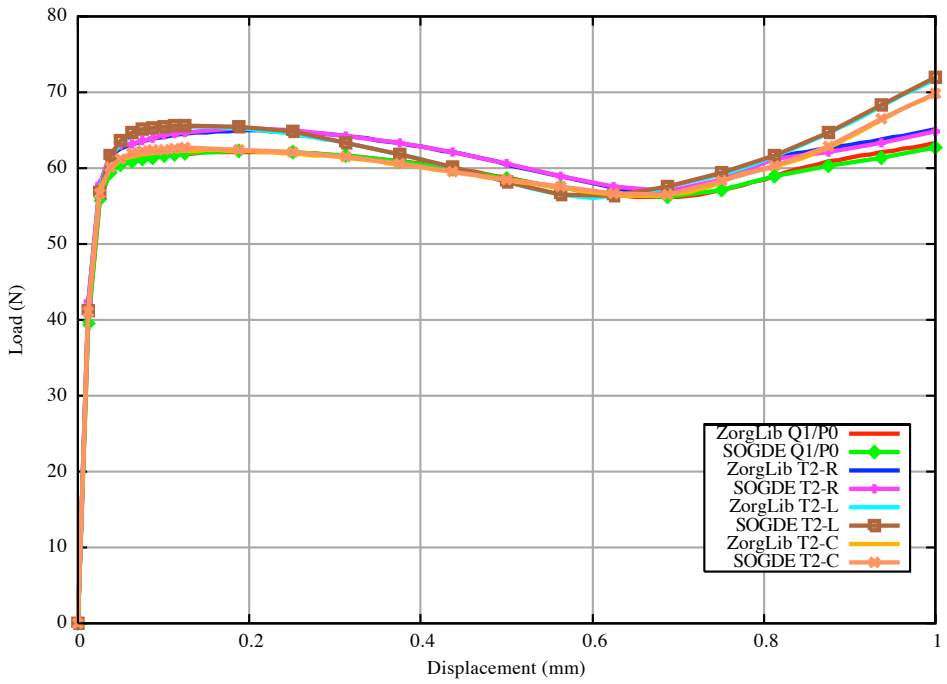

Figure 14: Load-displacement curves for different meshes and formulations

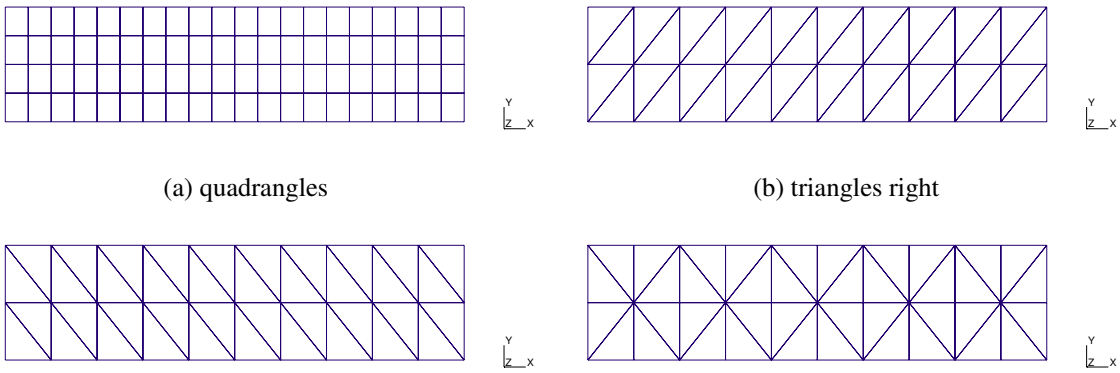

(a) quadrangles

(b) triangles right

(c) triangles left

(d) triangles crossed

Figure 15: Meshes for cylindrical billet

to a reduction in height of 32%. The resulting deformed shape and equivalent plastic strain distribution, obtained with ZorgLib, are shown in Figure 16, for the different meshes. In this plot, quadratic triangles have been subdivided in linear triangles for the purpose of representation.

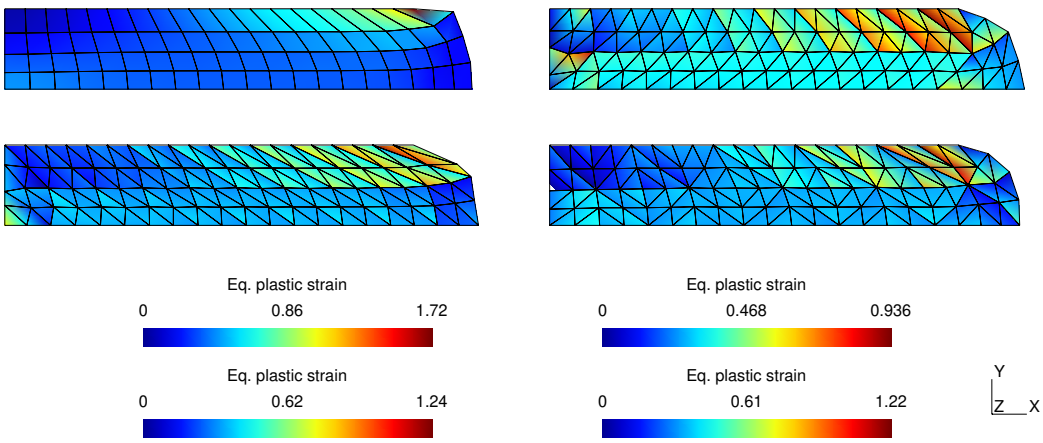

Figure 16: Deformed shape and equivalent plastic strain distribution for various meshes

Significant differences appear at the level of the upper right corner. Clearly, neither the quadrangular nor the left triangular mesh does allow to model correctly the rounding of the billet. The shape obtained with the crossed triangular mesh appears the most satisfying. Nonetheless, this effect is only local, as shown in Figure 17, which displays the superposition of the radial displacement fields obtained with the quadrangular mesh (worst) and the crossed triangular mesh (best). Clearly, both fields coincide for the most part and the difference becomes significant only in the last column of elements.

We can also look at macroscopic measures, such as the crushing force *vs.* displacement curves shown in Figure 18. We see that, in the case of the quadrangular elements, both formulations agree very well. But they differ significantly from results obtained with triangular meshes at high compression levels. In the case of triangular elements, the various arrangements of mesh do not lead to significant differences. Differences which appear (at high compression levels) seem to be linked to the formulation of the constitutive updates. A possible explanation

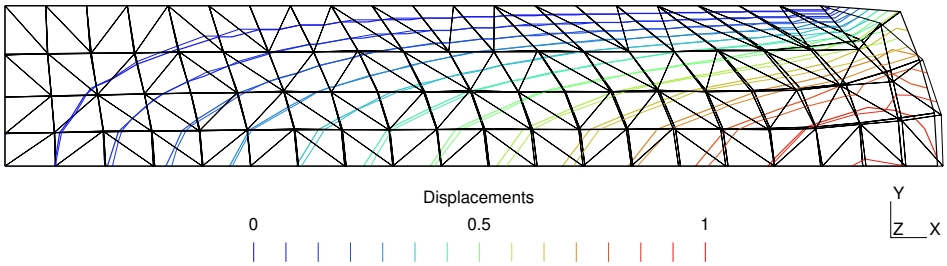

Figure 17: Radial displacement fields obtained with quadrangular and crossed triangular meshes

for this could be the importance of (elastic) volumic strains in this benchmark.

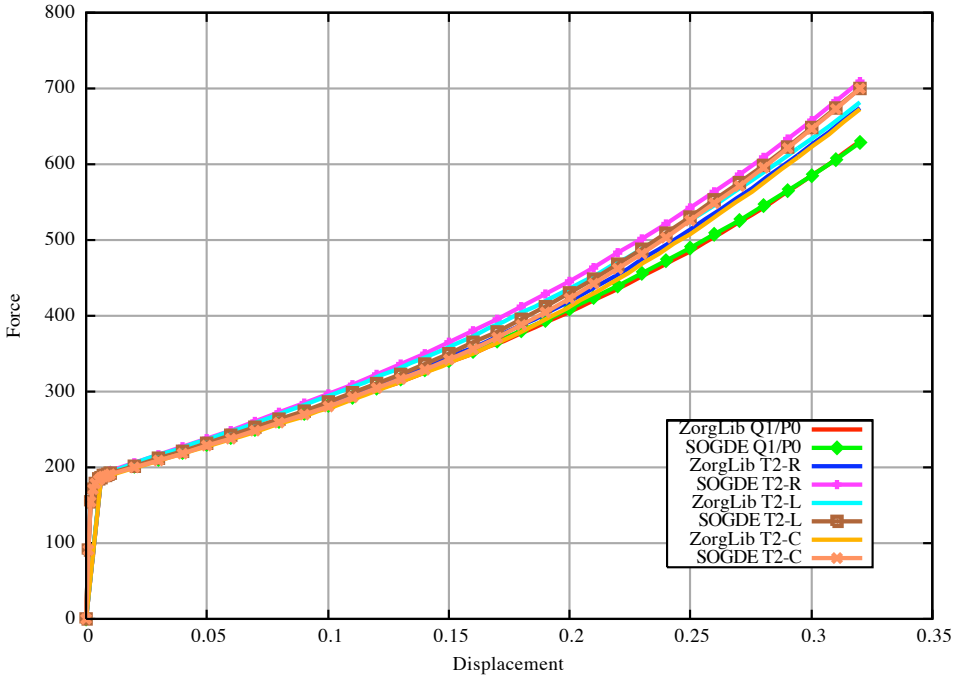

Figure 18: Load-displacement curves obtained from quadrangular and crossed triangular meshes with ZorgLib and SOGDE

8 CONCLUSIONS

The conclusions which can be drawn from the various numerical simulations run till now are:

- The differences in formulation between SOGDE and ZorgLib do not lead to significant variations in the results ;
- Quadratic 6-noded triangles provide a good alternative to bilinear quadrangles, even in the case of large plastic strains ;
- Bilinear quadrangles seem to lead to a stiffer model than quadratic triangles, at equivalent number of degrees of freedom. But this additional compliance of triangular meshes also leads to higher levels of distortion, especially in the case of fully unstructured meshes.

These high levels of distorsion can be detrimental to the quality of solution in terms of internal variable fields, while it seems to have little effect on macroscopic measures.

Further work should focus on more detailed comparisons, especially of stress and strain distribution. A fully 3-dimensional benchmark should also be considered.

REFERENCES

P.W. Bridgman. *Studies in large plastic flow and fracture, with special emphasis on the effects of hydrostatic pressure*. Harvard University Press, Cambridge, Massachusetts, 1964.

A.M. Cuitiño and M. Ortiz. Computational modelling of single crystals. *Modelling and Simulation in Materials Science and Engineering*, 1:225–263, 1992.

T.C. Doyle and J.L. Ericksen. Nonlinear elasticity. In H.L. Dryden and T. von Kàrmàn, editors, *Advances in Applied Mechanics*, volume 4. Academic Press, 1956.

A.L. Eterovic and K.-J. Bathe. A hyperelastic-based large strain elasto-plastic constitutive formulation with combined isotropic-kinematic hardening using the logarithmic stress and strain measures. *International Journal for Numerical Methods in Engineering*, 30(6):1099–1114, 1990.

F. Gabaldón. *Métodos de elementos finitos mixtos con deformaciones supuestas en elastoplasticidad*. PhD thesis, E.T.S. Ingenieros de Caminos. Universidad Politcnica de Madrid, Madrid, 1999.

C. García-Garino. *Un modelo numérico para el análisis de sólidos elastoplásticos sometidos a grandes deformaciones*. PhD thesis, E.T.S. Ingenieros de Caminos, Universidad Politécnica de Catalunya, Barcelona, 1993.

C. García-Garino, F. Gabaldón, and J. Goicolea. Finite element simulation of simple test in metals. *Finite Elements in Analysis and Design, in press*, 2006.

C. García-Garino, F. Gabaldón, J. Goicolea, A. Mirasso, and S. Raichman. Simulación computacional del ensayo de tracción simple con estricción (in spanish). `http://w3.mecanica.upm.es/papers/informe-hyper.pdf`, Proyecto PICT-12-03268. FONCYT. ANPCyT, 2004.

C. García-Garino and J. Oliver. Un modelo constitutivo para el análisis de sólidos elastoplásticos sometidos a grandes deformaciones: Parte 1 formulación teórica y aplicación a metales. *Revista Internacional de Métodos Numéricos para Cálculo y Diseño en Ingeniería*, 11:105–122, 1995.

C. García-Garino and J. Oliver. Un modelo constitutivo para el análisis de sólidos elastoplásticos sometidos a grandes deformaciones: Parte 2 implementación numérica y ejemplos de aplicación. *Revista Internacional de Métodos Numéricos para Cálculo y Diseño en Ingeniería*, 12:147–169, 1996.

J. Goicolea. *Numerical modelling in large strain plasticity with application to tube collapse analysis*. PhD thesis, University of London, 1985.

A.E. Green and P.M. Nagdhi. A general theory of elastic plastic continuum. *Archives Rational Mechanical Analysis*, 18:251–281, 1965.

E.H. Lee. Elastic-plastic deformation at finite strains. *Journal of Applied Mechanics*, 36(1): 1–6, 1969.

J. Lubliner. Thermomechanics of deformable bodies. Department of Civil Engineering, University of California, Berkeley, 1985.

J. Lubliner. *Plasticity Theory*. Macmillan Publishing Company, New York, 1990.

L.E. Malvern. *Introduction to the Mechanics of a Continuous Motion*. Prentice-Hall, 1969.

J.E. Marsden and T.J.R. Hughes. *Mathematical Foundations of Elasticity*. Prentice-Hall, 1983.

C. Miehe. Exponential map algorithm for stress updates in anisotropic multiplicative elastoplasticity for single crystals. *International Journal for Numerical Methods in Engineering*, 39 (19):3367–3390, 1996.

C. Miehe and E. Stein. A canonical model of multiplicative elasto-plasticity. formulation and aspects of the numerical implementation. *European Journal of Mechanics, A/Solids*, 11: 25–43, 1992.

J.-J. Moreau. Application of convex analysis to the treatment of elastoplastic systems. In P. Germain and B. Nayroles, editors, *Applications of Methods of Functional Analysis to Problems in Mechanics*. Springer-Verlag, 1976.

M. Ortiz and L. Stainier. The variational formulation of viscoplastic constitutive updates. *Computer Methods in Applied Mechanics and Engineering*, 171(3-4):419–444, 1999.

J.-P. Ponthot. *Traitement unifié de la Mécanique des Milieux Continus solides en grandes transformations par la méthode des éléments finis*. PhD thesis, University of Liège, Liège, Belgium, 1995.

R.T. Rockafellar. *Convex Analysis*. Princeton University Press, Princeton, New Jersey, 1970.

B. Schutz. *Geometrical Methods of mathematical physics*. Cambridge University Press, Cambridge, 1990.

J.C. Simo. A framework for finite strains elastoplasticity based on maximum plastic dissipation and the multiplicative decomposition. Part I: Continuum formulation. *Computer Methods in Applied Mechanics and Engineering*, 66:199–219, 1988a.

J.C. Simo. A framework for finite strains elastoplasticity based on maximum plastic dissipation and the multiplicative decomposition. Part II: Computational aspects. *Computer Methods in Applied Mechanics and Engineering*, 68:1–31, 1988b.

J.C. Simo and M. Ortiz. A unified approach to finite deformation analyisis based on the use of hyperelastic constitutive equations. *Computer Methods in Applied Mechanics and Engineering*, 49:222–235, 1985.

G. Weber and L. Anand. Finite deformation constitutive equations and a time integration procedure for isotropic hyperelastic-viscoelastic solids. *Computer Methods in Applied Mechanics and Engineering*, 79(2):173–202, 1990.